(Received 6 January 2025, Accepted 16 March 2025, Scheduled 3 April 2025)

Design of Absorption-Scattering Integrated Multi-Layer Metasurfaces for Large-Angle Anomalous Reflection

Jie Zhang[1,2], Wangchang Li[1,2], Yue Kang[3], Ting Zou[3], Xiao Han[3], Yao Ying[1,2], Jing Yu[1,2], Jingwu Zheng[1,2], Liang Qiao[1,2], Juan Li[1,2], Faxiang Qin[4,*], and Shenglei Che[1,2,*]

[1] *College of Materials Science and Engineering, Zhejiang University of Technology, Hangzhou 310014, China*
[2] *Research Center of Magnetic and Electronic Materials, Zhejiang University of Technology, Hangzhou 310014, China*
[3] *Systems Engineering Institute, Beijing, 100010, China*
[4] *College of Materials Science and Engineering, Zhejiang University, Hangzhou 310058, China*

ABSTRACT: This paper presents a novel absorption-scattering integrated multilayer metasurface (ASIMMS) designed to effectively control the propagation and absorption of electromagnetic waves. Special attention is paid to the efficient suppression of abnormal reflection and parasitic reflection under oblique incidence conditions. The research achieved highly efficient beam coupling in the desired direction by precise impedance modulation and excitation of an appropriate set of evanescent wave patterns. The high conductivity of multi-walled carbon nanotube films (MWCNTFs) is used to enhance the localization of electromagnetic field within the metasurface, thereby improving the absorption efficiency. The experimental results show that the designed ASIMMS achieves 86.8% electromagnetic wave absorption, 11.1% expected directional reflection efficiency, and 97.9% absorption-scattering efficiency at the operating frequency of 10 GHz under 15° oblique incidence. This method proficiently controls both direction and magnitude of scattering while effectively utilizing any diffraction order, paving the way for innovative applications in beam manipulation, stealth technology, and electromagnetic shielding.

1. INTRODUCTION

With the advancement of electronic information technology [1, 2], electromagnetic warfare has propelled the transformation of new military technologies [3]. In more complex application environments, such as flat plate structures [4, 5], large conical structures, cabin structures [6], and leading edges of wings, there are more intricate demands for the absorption [7], reflection [8, 9], and transmission [10] of electromagnetic (EM) waves. Consequently, extensive research [12, 13] has been dedicated to the development of new types of electromagnetic materials and design strategies to achieve more efficient and covert control of EM waves [14]. Metasurfaces possess immense beam manipulation capabilities [15–17], including the absorption of plane waves and the reflection/refracting them into anomalous directions. This necessitates the meticulous design of subwavelength meta-atoms in each period of the metasurface [18, 19], which ensures the singular coupling to the desired Floquet-Bloch modes, or equivalently, suppresses the parasitic reflection (i.e., the energy of the incident electromagnetic wave coupling to the other modes [20]). However, in reflecting, absorbing, and polarizing EM waves with a given plane wave incident normally [21, 22], the efficiency of traditional electromagnetic metasurfaces is limited by the constraints of the materials used as per the generalized Snell's law [23, 24]. It is also highly sensitive to the incidence angle [25], and the control of high efficient beam can achieve only at a limited reflection angle [26].

However, achieving large-angle anomalous reflection of EM waves and dissipating parasitic reflection from other channels under oblique angles of incidence necessitates metasurfaces with more flexible control capabilities for impedance modulation, thereby increasing the complexity of their design. By using lossy materials such as graphene, carbon nanotube films, and ITO films in metamaterials, it is possible to achieve highly efficient broadband absorbers [27] and multi-channel absorbers [28]. Tan et al.'s [7] analytical design method for a perfect absorber based on metagratings rigorously examines the supercells of metagratings using established theory, derives specific load impedance density expressions, and achieves absorption of over 90% of electromagnetic waves. However, the absorber is still sensitive to the incidence angle, causing a decrease in the absorption efficiency. Perfect control of the beam can be achieved by designing a complex multi-layer structure [29, 30], sandwich structures [31], etc. to obtain more degree of freedom for impedance modulation [32, 33]. In contrast, the introduction of evanescent wave mechanisms plays a crucial role in the impedance design of high-performance metasurfaces. Epstein and Eleftheriades [34] proposed multi-layer penetrable bi-anisotropic omega units and incorporated auxiliary fields to flexibly and efficiently achieve EM waves reflection, beam splitters, abnormal transmission, and other functions. D□az-Rubio et al. [35], based on leaky wave antenna theory, designed appropriate leaky modes to effectively redi-

* Corresponding authors: Faxiang Qin (faxiangqin@zju.edu.cn); Shenglei Che (cheshenglei@zjut.edu.cn).

rect the incident wave to the desired diffraction pattern, and experimentally demonstrated an efficiency of 94%. Zhong et al. [36], based on transmission line theory, optimized the admittance matrix Fourier coefficients of the meta-grating to excite a set of unidirectional evanescent wave modes to achieve coherent perfect absorption of shock waves from any asymmetric direction. However, none of these studies considered situations in which oblique incidence, the impedance mismatch, causes parasitic reflection. In terms of electromagnetic properties, the conductivity and EM wave absorption performance of carbon nanotubes are intricately linked to their structure, morphology, and defects [37]. Owing to their distinctive structure and properties such as high specific surface area, low density, and exceptional electromagnetic performance, Carbon nanotubes [38] exhibit significant potential in the field of EM wave regulation. Consequently, it is possible to use carbon nanotube materials, with more accurate impedance modulation methods, to design non-reciprocal or reciprocal, effective absorption-scattering integrated metasurfaces over an oblique angle of incidence.

In our study, to address the challenge of effectively suppressing parasitic reflection and achieving high anomalous reflection efficiency at large angles under oblique incidence of electromagnetic waves, we proposed an absorption-scattering integrated multi-layer metasurface (ASIMMS). We carefully conducted a comprehensive analysis of the Floquet harmonic power of all possible orders and carefully examined the impedance density distribution of the metasurface. Through this investigation, we have identified an optimal excitation method for evanescent waves to improve the efficiency of beam coupling and EM wave absorption. Based on this theoretical foundation, we prepared a multi-walled carbon nanotube film (MWCNTF) on a grounded dielectric substrate. By utilizing its high conductivity and loss characteristics, as well as changing the geometric parameters of the structure, we enhanced the localization of the electromagnetic field on the metasurface, thereby achieving finer control over it and affecting its absorption and scattering properties. Our simulated and experimental results show that our designed ASIMMS achieves the EM wave absorption rate $A = 86.8\%$, the efficiency of 11.1% for expected direction reflection $\theta r = 62.5°$, and the absorb-scatter efficiency reaching 97.9% at a working frequency of 10 GHz with 15° oblique incidence. This result emphasizes the robustness of our semi-analytical approach and confirms the effectiveness in designing multifunctional absorb-scatter integrated electromagnetic metasurfaces. This method proficiently controls both the direction and magnitude of scattering while effectively utilizing any diffraction order, paving the way for innovative applications in beam manipulation and control.

2. MATERIAL

Figures 1(a) and (b) depict a multi-walled carbon nanotube film (MWCNTF) with dimensions of 380 mm × 220 mm and a thickness of merely 20 µm which is continuously deposited from multi-walled carbon nanotubes (MWCNTs). The MWCNTF can be regarded as a conductive network formed by the interweaving of countless carbon nanotubes (Figure 1(c)), where individual MWCNTs consist of concentrically nested carbon nanotubes. MWCNTs can possess a high degree of order and three-dimensional crystallinity. Each cylindrical shell or wall of MWCNTs is perfectly nested within the structure, with an interlayer spacing similar to that between planes in crystalline graphite. In MWCNTs, electron transport primarily occurs in the outermost layer. Electrons in the inner layers can interact with those in the outer layer through mechanisms such as tunneling effect, Coulomb drag, and diffusion scattering, although these interactions are relatively weak. The internal fine structure of the carbon nanotube film was investigated through scanning electron microscopy (SEM) characterization. The micromorphological characteristics of the MWCNTF are depicted in Figure 1(d), illustrating how each MWCNT establishes conductive channels as part of the overall conductive network. Its conductivity is influenced by a range of factors, including nanotube diameter, number of walls, defect density, and crystallinity [39].

The ratio of the D peak to the G peak (I_D/I_G) serves as a crucial parameter for evaluating the crystal purity and defect density of carbon nanotubes, as depicted in Figure 1(e). The presence of the D peak is indicative of defects within the carbon nanotubes, while the G peak is representative of their graphitic structure, reflecting the planar vibration mode of carbon atoms. The Raman IG/ID ratio for the MWCNT sample stands at 0.42, signifying a relatively high level of purity with only minimal defects such as irregularly arranged carbon atoms, amorphous carbon, end points, and wall defects. These imperfections may contribute to additional interface polarization and increased surface area, thereby providing more pathways for electron transport and influencing electrical properties and conductivity; heightened electron mobility and scattering centers offer an abundance of pathways and interfaces that facilitate absorption and scattering of EM waves as they traverse through the material.

MWCNTs possess high conductivity and absorption properties, which make them particularly effective at exciting surface plasmon polarizations (SPPs) [40]. SPPs occur when EM waves interact with the free electrons on the surface of materials, leading to an enhanced localization effect of the electromagnetic field. Based on the Drude model and binary Green's function [41] (Figures 1(f), (g)), the local electromagnetic characteristics of MWCNTs were simulated. The distribution of electric field intensity within MWCNTs, which are formed by the random distribution of multiple roots, was simulated using transition boundary conditions (with the material conductivity set to 7×10^4 S/m, wall thickness $s = 0.34$ nm, and the diameter of the MWCNT $d = 40$ nm). Observing each multi-walled carbon nanotube, an electric field concentration effect is noted near the surface and tip of the nanotube; between adjacent MWCNTs with a closely packed structure, a significantly high electric field intensity is observed, and the EM wave transmission-reflection coefficient (T-R) of the MWCNT is substantially influenced by the distance (r) between neighboring tubes. This localized electric field enhancement effect can improve the performance of carbon nanotubes in applications such as electron emission, sensing, and optoelectronic devices.

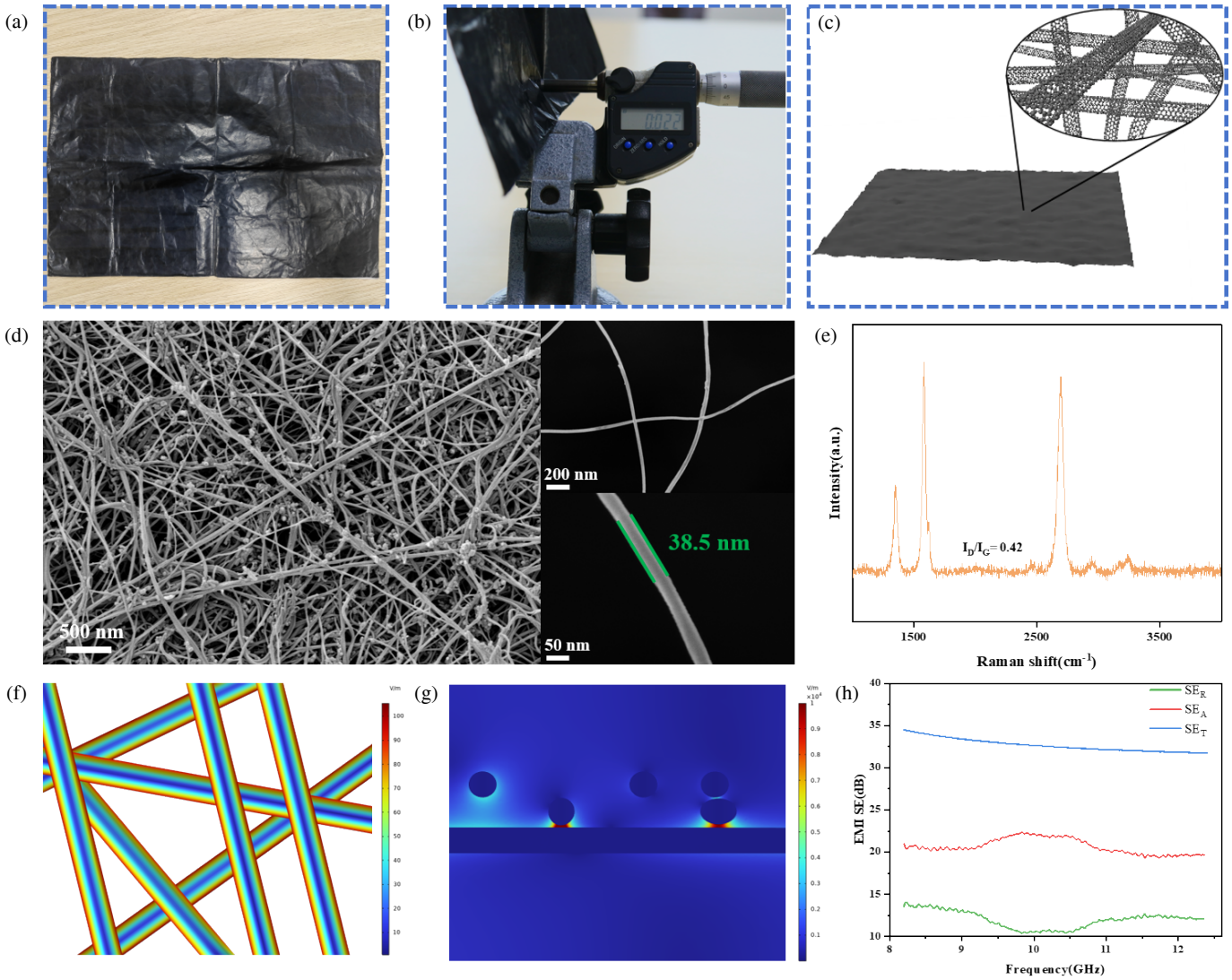

FIGURE 1. Characterization analysis of carbon nanotube membrane: (a) digital image of lightweight MWCNTF; (b) measurement of the thickness of the MWCNTF; (c) schematic diagram depicting the conductive network formed by interweaving MWCNTs; (d) SEM image showing the morphology of the MWCNTF; (e) Raman spectroscopy results, including ID and IG values; (f), (g) electric field intensity diagrams simulated using COMSOL; (h) electromagnetic interference shielding effectiveness (EMI SE), shielding effectiveness in absorption (SE$_A$), transmission (SE$_T$), and reflection (SE$_R$).

In the EMI shielding performance of MWCNTF, absorption efficiency (SE_A) is the main contributing factor, while the effects of multiple reflections (SE_M) and surface reflections (SE_R) are relatively minor. As shown in Figure 1(h), the SE_A value averages at approximately 32.6 dB within the 8.2–12.4 GHz frequency range, where the proportion of SE_A in SE_T is about 67.5%. However, the conductive properties of a single MWCNT film can lead to the significant reflection of incident EM waves, making it unsuitable for absorbing and attenuating millimeter wave EM waves. To address this issue, the MWCNT film is integrated into a metasurface design, leveraging its high conductivity to enhance the absorption of EM waves by exciting surface plasmon polaritons and subsequent localization of the electric field. This design strategy not only reduces reflective losses but also improves the overall EMI shielding effectiveness of the MWCNTF. The high electrical conductivity of the MWCNTF, in conjunction with its structured integration into the metasurface, facilitates efficient absorption of EMI, attenuation of incident waves, and reduction of electromagnetic interference in diverse integrated optical applications.

3. DESIGN THEORY

Figure 2 illustrates the fundamental design concept of the proposed absorption-scattering integrated multi-layer metasurface (ASIMMS) based on a lossy medium. In this work, we use surface impedance model as the homogenization model for the ASIMMS, which is an impenetrable reciprocal lossy metasurface with periodic modulation along the x-direction of the surface, with a period of Dx. Let us assume that an incident plane wave with a field (E_i, H_i)

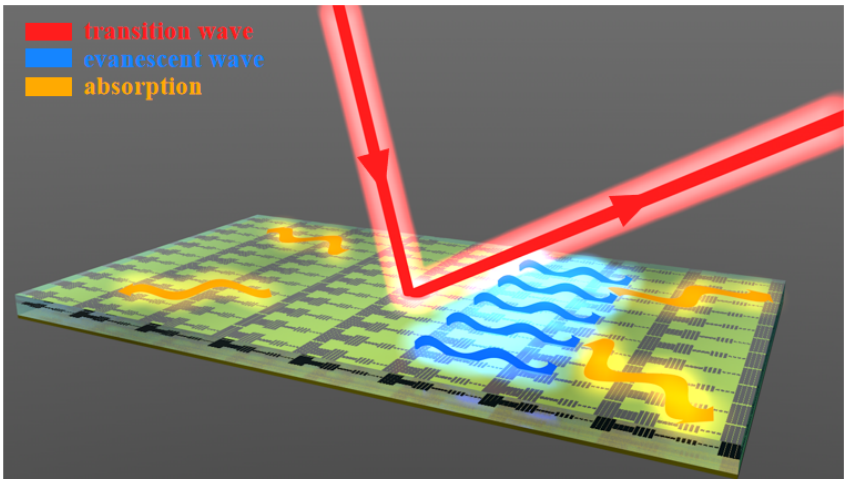

FIGURE 2. Reconfiguring the surface impedance analytically for a single period to achieve ASIMMS for both incident and reflected beams with (θ_i, θ_r).

strikes the xoy plane at an angle θ_i, and the energy is distributed only into the channel at angle $\theta_i = \theta_r$, as a reflected plane wave with a field (E_r, H_r). Assuming and suppressing the $e^{j\omega t}$ time convention, the tangential components of the total electric field at the plane $z = 0$ can be written as $E_{tot}(x) = E_0\left(e^{-jk_0 \sin\theta_i x} + A_r e^{-jk_0 \sin\theta_r x}\right)$. The corresponding total magnetic field reads $H_{tot}(x) = \frac{E_0}{\eta}\left(\cos\theta_i e^{-jk_0 \sin\theta_i x} - \cos\theta_r A_r e^{-jk_0 \sin\theta_r x}\right)$, where E_0 is the E-field amplitudes for the incident plane wave, and A_r is the E-field amplitudes for the reflected plane wave, which ranges between 0 and $\sqrt{\cos\theta_i/cos\theta_r}$. Here, k_0 and η are the wave number and impedance in free space. The desired electromagnetic properties to achieve this ideal MMS can be characterized by a nonuniform scalar surface impedance, which defines the relationship between the surface average tangential electric field and magnetic field on the metasurface. After determining the incident field, reflected field, and transmitted field of the metasurface, this surface impedance represents the ratio of the tangential electric field to the magnetic field at the surface $Z_s(x) = E_{tot}(x)/H_{tot}(x)$.

It is worth noting that the surface impedance is typically a complex function, composed of both real and imaginary parts. As shown in Figures 3(a) and 3(b), we take a set of incidence and reflection beams with $(\theta_i, \theta_r) = (15°, 62.5°)$ as an example to analyze the variation patterns of the real and imaginary parts of the surface impedance with the change in the amplitude of the reflected field. It can be clearly observed that both the real and imaginary parts of the impedance surface decrease as the amplitude of the reflected field diminishes, causing the surface to flatten along the period. The real part of the impedance periodically takes positive (corresponding to loss) and negative (gain) values, while the variation of the imaginary part directly affects the phase delay of the metasurface to the EM wave, which can be used to design metasurface structures with specific phase responses, such as applications in holographic display or wavefront control. Recently, study [42] has shown that, in principle, metasurfaces capable of anomalous reflection can be realized, meaning that there is no parasitic reflection, scattering, or absorption.

In order to achieve perfect anomalous reflection, the power carried in the desired direction should be equal to the power of the incident plane wave. Therefore, the amplitude of the reflected wave can be calculated as $A_r = \sqrt{\cos\theta_i/\cos\theta_r}$. Taking this condition into consideration, the surface impedance can be expressed as

$$Z_s(x) = \frac{\eta}{\sqrt{\cos\theta_i cos\theta_r}} \frac{\sqrt{\cos\theta_r} + \sqrt{\cos\theta_i} e^{j\varphi_r(x)}}{\sqrt{\cos\theta_i} - \sqrt{\cos\theta_r} e^{j\varphi_r(x)}} \tag{1}$$

where $\varphi_r(x) = k_0(\sin\theta_i - \sin\theta_r)x$. The absorption of energy by the metasurface can effectively inhibit parasitic reflection, which is the result of the interaction between EM waves and metasurface. This interaction causes reflection and scattering within the material, resulting in increased energy dissipation and ultimately a reduction in the amplitude of the reflected field. Asadchy et al. [43] and Estakhri and Alù [23] showed that when $Er = Ei$ $(Ar = 1)$, the solution of Maxwell's equations generates a corresponding surface impedance as:

$$Z_s(x) = Z_0 \frac{1 + e^{j\varphi_r(x)}}{\cos\theta_i - \cos\theta_r e^{j\varphi_r(x)}} \tag{2}$$

As an example, we consider an incident wave with the incidence angle of $\theta_i = 15°$, and the incident power is reflected into an anomalous reflection angle of $\theta_r = 63°$. Then, based on the surface impedance given by Equation (1) and Equation (2), we designed a lossless gradient metasurface (LGMS) and a Lossy surface impedance modulated metasurface (LSIMMS). As shown in Figure 3(c), the key idea is to retrieve the surface impedance of the target device by matching the boundary conditions on the metasurface with the incident and output waves. The presence of periodic oscillations in $R(Z_s(x))$ indicates that the local structural materials making up the metasurface must be gain or loss materials, a feat that is exceedingly challenging to accomplish in practical applications [35].

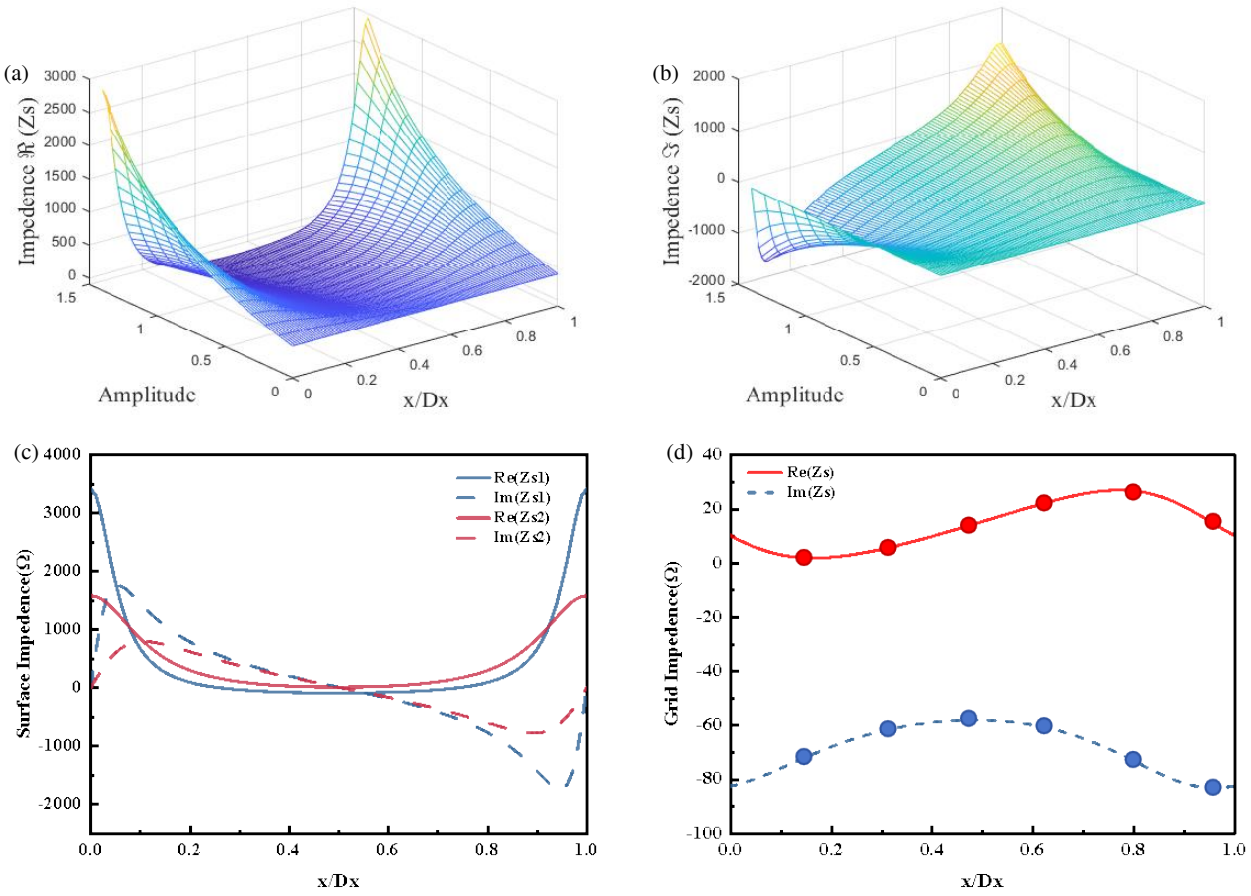

FIGURE 3. Under different reflection amplitudes A_r, $\theta_i = 15°$, $\theta_r = 62.5°$, the distribution of surface impedance (a) real part; (b) imaginary part; (c) the surface impedance curves corresponding to equations 1 and 2; (d) obtain the surface impedance curve of ASIMMS.

Now we discuss how the ASIMMS can excite the appropriate evanescent wave. Since the metasurface is periodically modulated with the period Dx, the gradient surface will scatter into an infinite number of Floquet harmonics. The tangential wave vector of the Floquet modes can be written as $k_{xn} = k_0 \sin\theta_i + n\,(2\pi/Dx)$, where n is the mode order of the harmonic. The corresponding normal component of the reflected wave number equals $k_{rzn} = \sqrt{k_0^2 - k_{rxn}^2}$. If $|k_{rxn}|$ is greater than the incident wavenumber, the wave is evanescent, and it does not contribute to the far field. For the harmonic wave satisfying $|k_{rxn}| < k_0$, k_{rzn} is real, and this wave is propagating. The evanescent harmonics will be dissipated by the lossy surface, and the propagating harmonics will propagate into the far zone at the angle θ_n, defined as

$$\theta_n = \arcsin\left(\sin\theta_i + \frac{n\lambda}{Dx}\right) \tag{3}$$

where λ stands for the wavelength.

To further analyze the mechanism by which evanescent waves modulate the surface impedance of ASIMMS, we can utilize the method reported in [44]: For incidence on a single port, we define the scattering propagation modes in the desired S-matrix and a set of evanescent harmonics with unknown complex amplitudes. Here, we set the incident wave as the 0th order mode, and the reflected wave as the first-order mode of the entire periodic system. We optimize the Fourier coefficients of the impedance distribution until the optimized surface produces the required propagation harmonics upon multiple incidences. The optimized surface activates a set of appropriate auxiliary evanescent modes. Consequently, due to the spatial periodicity of the surface, the surface impedance $Zs(x)$ or admittance $Ys(x) = 1/Zs(x)$ can be expanded into a Fourier series, such as:

$$Z_s(x) = \sum_{m=-\infty}^{+\infty} c_n e^{-jn\beta_M x}$$

or (4)

$$Y_s(x) = \sum_{m=-\infty}^{+\infty} g_n e^{-jn\beta_M x}$$

where c_n and g_n are the Fourier coefficients of the impedance and admittance functions, respectively. We can see that the admittance matrix Y_s is determined only by the Fourier coefficients of the modulation function, filled in the r and columns $Y_s(r,c) = g_{r-c}$. Alternatively, the surface can be characterized by the Toeplitz impedance matrix Z_s, filling in the Fourier term of $Z_s(x)$, i.e., $Z_s(r,c) = c_{r-c}$.

TABLE 1. Numerical results and comparison between the different design possibilities for metasurface. Power of waves sent into the respective directions, absorption coefficient, and power efficiency.

	Parasitic reflection	Desired reflection	Absorption	Efficiency
Lossless gradient metasurface (by scheme 1)	99.3%	0.7%	0%	0.7%
Lossy surface modulated metasurface (by scheme 2)	40.55%	1%	58.45%	59.45%
Absorption-scattering integrated multi-layer metasurface (in scheme 3)	2.1%	11.1%	86.8%	97.9%

Next, We calculate the impedance matrix for the dielectric plate Z_d. Since there is no modulation in the dielectric layer, there are no coupling terms (non-diagonal terms) in the characteristic impedance matrix of the dielectric Z_d. The matrix only contains diagonal terms $Z_d(n,n)$ (rows and columns of the matrix from $-N$ to $+N$), where $Z_d(n,n)$ represents the characteristic impedance of n harmonics. The characteristic impedance of TE polarization can be expressed as

$$Z_d^{TE}(n,n) = \frac{\mu_0\omega_0}{k_{zn}^d}. \tag{5}$$

where $k_{zn}^d = \sqrt{\omega_0^2\varepsilon_0\varepsilon_d\mu_0 - k_{xn}^2}$ is the normal component of the wave vector in the dielectric, and ε_d and h are the permittivity and thickness of the substrate, respectively. The reflection matrix is calculated as $\Gamma = (Y_0+Y_s+Y_d)^{-1}(Y_0-Y_s-Y_d)$, where Y_s is the grid admittance matrix, which is a Toeplitz matrix determined by the Fourier coefficients (see Equation (S23), Supporting Information of [44]).

To achieve high beam coupling and absorption efficiency in ASIMMS, it is essential to consider the fundamental parameters of MWCNTF and the medium thickness as additional design variables. The complexity of matrix operations makes it straightforward to solve for grid impedance and substrate parameters, as the conduction of the foundation plate with medium thickness is closely linked to the harmonic number. Therefore, an optimal solution for grid impedance distribution and substrate thickness can be obtained through a mathematical optimization algorithm based on scattering matrix analysis. In contrast to previous studies [12, 45, 46] on metamaterials, the simultaneous achievement of expected performance in ASIMMS is attributed to multi-wall carbon nanotube thin films (MWCNTFs), surface impedance modulation (SIM), and appropriate evanescent wave excitation. This approach enables the absorption of electromagnetic wave energy, complete suppression of lateral lobe, and effective control of scattering beam direction.

The red and blue lines in Figure 3(d) represent the real and imaginary components of the surface impedance distribution as defined by the equations $Y_s(x) = g_0 + g_1 e^{-j2\pi x/Dx}$, respectively, with $g0 = (2.472 + 1.257) * 10^{-3}$, $g1 = -(1.272 + 1.216) * 10^{-3}$, frequency $= 10$ GHz, $\theta_i = 15°$, and $\theta_r = 62.5°$. However, the analytical estimation of the ideal impedance curve is merely an approximation due to the utilization of a uniform impedance model assuming homogeneity at wavelength scales. Therefore, we employ a discretization method to numerically optimize the surface impedance for a more precise profile, as illustrated in Figure 3(d), with red and blue dots representing uniform reactive surface units. As predicted by the aforementioned theory, capacitance is consistently present, increasing during one half of the cycle and decreasing during the other. The deviation in anticipated values from the analytical model can be attributed to its approximation, primarily due to periodic boundary conditions applied to cells resulting in a more complex evanescent field structure than that assumed in the analytical analysis. The optimization of grid impedance can be achieved by adjusting both resistance and capacitance values. Here, an MWCNTF with a sheet impedance of 0.7 Ωsq-1 was employed, enabling the customization of grid resistance and reactance separately through the creation of a consistent resistive film. During the design process, increasing grid resistance can be achieved by reducing the width of strip W. Additionally, control over patch width is possible by adjusting the length L between adjacent cells and changing the patch gap between adjacent units. Therefore, the fine-tuning of strip width W was used to correct the grid resistance. Following these guidelines, these six unit cells were optimized one by one. In accordance with these recommendations, the six unit cells were individually optimized. The structural parameters for each sub-cell can be detailed in Table S3 (Section S3). It is evident that the impedances of all sub-cells closely align with the target values.

4. PHYSICAL IMPLEMENTATION AND EXPERIMENTAL VALIDATION

To demonstrate the absorption and scattering performance of the metasurface, we conducted full-wave simulations using the commercial software CST Microwave Studio 2020. As shown in Figures 4(a)–(c), for the three aforementioned schemes (see Table 1), the period of the three different metasurfaces can be calculated as 64 mm, and the numbers of discretized units in the unit cells are 8, 6, and 6, respectively. All metasurfaces comprise 6×11 sub-arrays, with the same total size of $384 \times 220\,\text{mm}^2$. The dielectric substrate in scheme 1 is SiO_2 with a relative permittivity of 3.94 and a loss tangent of 0.0002, and in the scheme 2 and 3 it is PMMA with a relative permittivity of 2.65 and a loss tangent of 0.0057. At the operating frequency of 10 GHz, Figures 4(d)–(e) display 2D far-field scattering patterns of the three different metasurfaces, with three propagating channels at $-21.5°$, $15°$, and $62.5°$, and the corre-

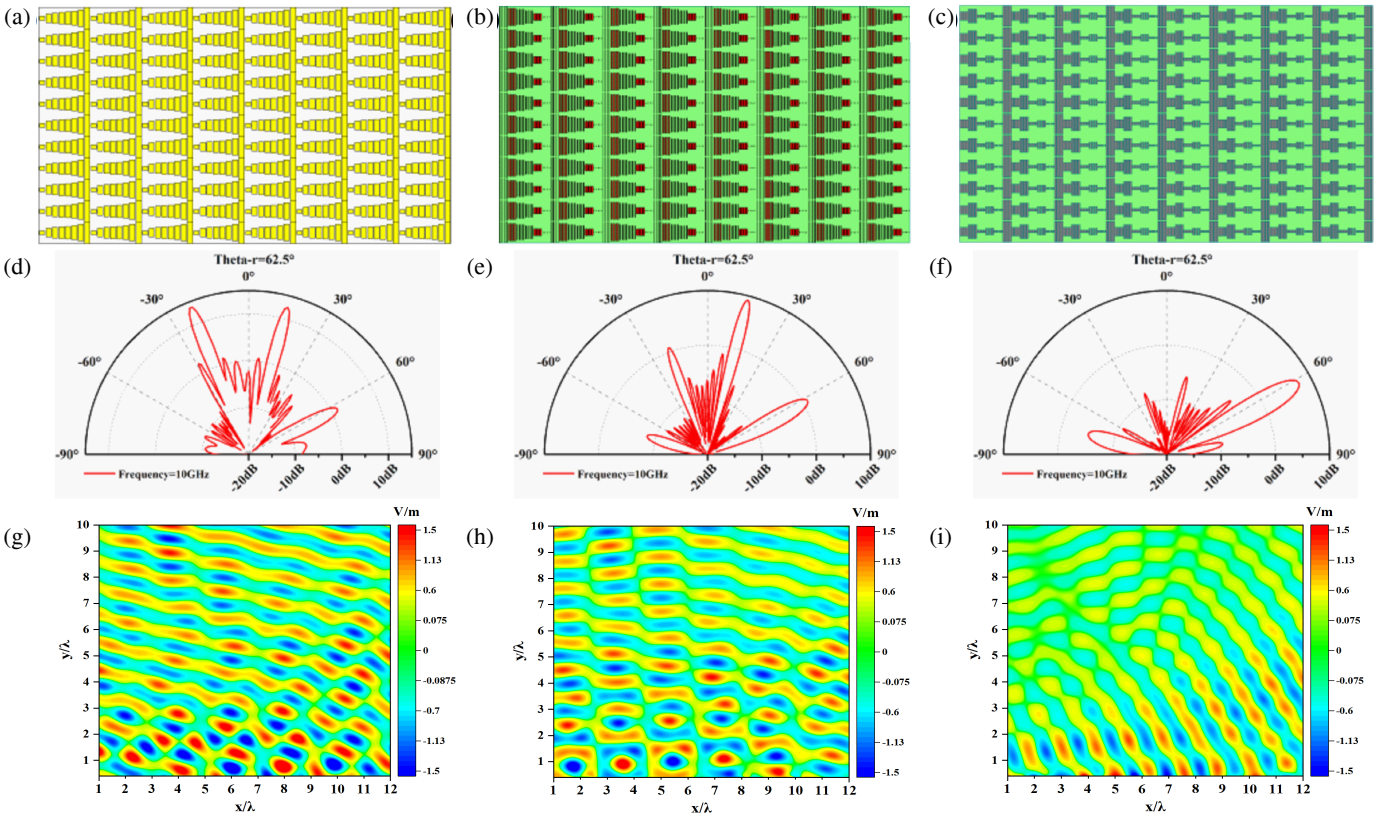

FIGURE 4. Schematic diagram of (a) LGMS; (b) LSIMMS; (c) ASIMMS; the scattering pattern of (d) LGMS; (e) LSIMMS; (f) ASIMMS; real part of the scattered electric field (g) LGMS; (h) LSIMMS; (i) ASIMMS.

sponding three theoretical diffraction patterns ($n = -1$, 0, and 1). For scheme 1, as shown in Figure 4(d), there are three directions in the scattered wave beams, but most of the power is reflected along the directions at $-21.5°$ and $15°$ ($n = -1$, 0). The energy of the incident wave cannot be coupled to the desired direction, and as predicted, the energy of EM wave is also not absorbed. This is because when the incident angle is oblique and the reflection angle θ ($\theta i + \theta r$) $> 75°$, if the metasurface design only considers the local response and phase factors of the unit structure, then the reflection efficiency will be significantly reduced. However, in scheme 2, as shown in Figure 4(e), we designed a lossy metasurface with impedance periodic modulation, which also has the same three theoretical diffraction channels. The energy in the mirror direction is reduced by 10 dB compared to scheme 1, and more energy is coupled to the $n = 1$ order channel. This illustrates that the design of the metasurface impedance distribution relies on the synergistic control of amplitude and phase. By utilizing the absorption capability of the lossy metasurface for EM waves, the energy of parasitic reflections can be reduced, and more energy can be coupled to the desired direction.

Therefore, by exciting the appropriate evanescent waves, the ASIMMS can achieve efficient anomalous reflection and suppress side lobes, as shown in Figure 4(f). Most of the power is reflected along the desired direction of $15°$ ($n = 1$), and the energy of other parasitic reflections ($n = -1, 0$) is negligible. The results indicate the ability of surface waves to propagate along the ASIMMS to redirect energy and achieve the perfect ideal "absorption-scattering integration" behavior. Furthermore, to further analyze the influence of evanescent waves on the propagation modes of the metasurface in near-field coupling, we conducted a numerical simulation of the electric field distribution of the designed metasurface. Figures 4(g)–(i) describe the scattered electric field in the xoz plane of the EM wave at a working frequency of 10 GHz, with θi=15° incidence for LGMS, LSMMMS, and ASIMMS. It is clear that the LGMS and LSIMMS designed according to scheme 1 and scheme 2 couple less energy to the desired direction, and parasitic reflections interfere with the desired reflection. The real part of the scattered electric field of the LGMS is shown in Figure 4(g), where the plane wave propagates along the mirror direction of the incident wave. As shown in Table 1, the reflection efficiency of this metasurface in the desired direction ($n = 1$) is $\xi_r = \left(\frac{E_r}{E_i}\right)^2 \cos\theta_r / cos\theta_i = 0.7\%$; the efficiency of parasitic reflections ($n = -1$, 0) is $\xi_r^{'} = 99.3\%$; and the absorption efficiency is $A = 1 - \xi_r - \xi_r^{'} = 0\%$. The impedance given by Equation (2) is a complex number with some positive real numbers, and its period is the same as the traditional design (by Eq. (1)). The real part of the surface impedance represents the loss of the metasurface, and the real part of its scattered electric field is shown in Figure 4(h). We can see that waves in three directions interfere with each other and fail to form a complete plane wave. The reflection efficiency of this metasurface for $n = 1$ order is

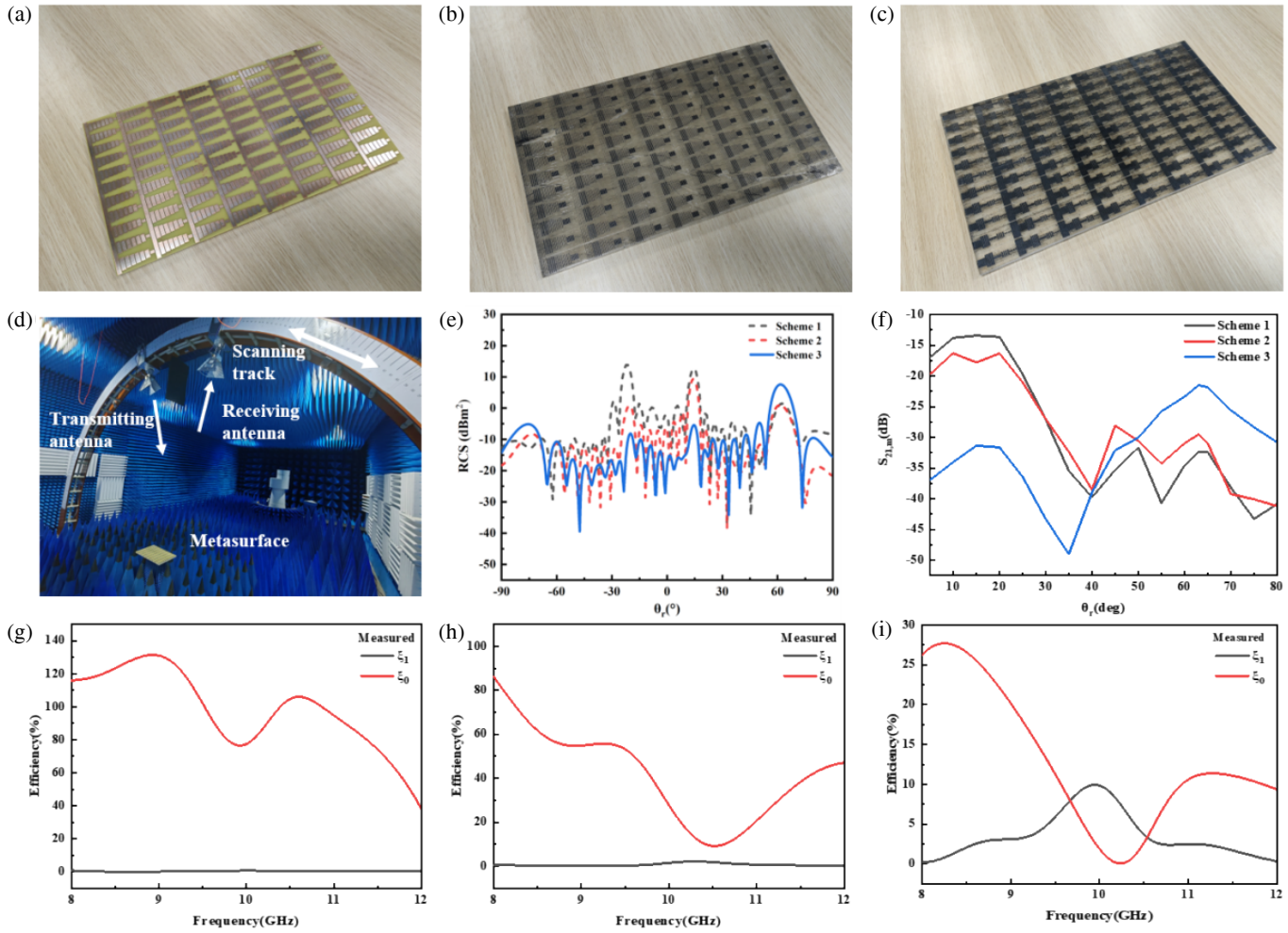

FIGURE 5. Experimental verification. Fabricated metasurfaces of (a) LGMS; (b) LSIMMS; (c) ASIMMS; (d) Experimental setup in an anechoic chamber. Signals measured by the receiving antenna for different orientation angles θ_r; (e) the 2D farfield pattern simulation diagram; (f) Signals at 10 GHz measured by the receiving antenna at different orientation angles with the transmitting antenna at 15°; measured reflection efficiency spectrum for different diffracted modes at 15° (red lines) and 62.5° (blue lines) (g) LGMS; (h) LSIMMS; (i) ASIMMS.

ξ_r= 1%; the efficiency for $n = -1$, 0 orders is ξ'_r= 40.55%; and the absorption efficiency is $A = 58.45\%$. When the metasurface is illuminated by an oblique incidence ($\theta i = 15°$), only Eq. (3) produces an almost perfect plane wave, whose propagation direction is indicated by a white arrow, and a surface wave propagating along the surface can also be formed. The real part of the scattered electric field is shown in Figure 4(i), where the efficiency for $n = 1$ order is $\xi_r = 11.1\%$; the amplitudes of the scattering propagation modes for $n = -1$ and 0 orders are close to zero; their efficiency is ξ'_r= 2.1%; the absorption efficiency is $A = 86.8\%$; and the absorption-scattering efficiency is 97.9%, meeting the expected functionality of the aforementioned ASIMMS.

In order to experimentally validate the aforementioned theories, we fabricated three samples, A, B, C, corresponding to the three schemes at 10 GHz using printed circuit board technology and laser etching technology (see Experiment Section), as shown in Figures 5(a)–(c). Sample A contains a 6×11 array with dimensions of $384 \times 220\,\text{mm}^2$ ($12.8 \times 7.3\lambda^2$). Copper foil was deposited on an FR4 substrate with a dielectric constant of $\varepsilon_r = 4.2$ via printed circuit board technology and pasted onto a SiO_2 board, with an aluminum board of the same size on the bottom, as shown in Figure S1. Samples B and C also contain 6×11 arrays with dimensions of $384 \times 220\,\text{mm}^2$. We used a copper foil/FR4 substrate and MWCNTF with a surface resistance of $0.7\,\Omega\text{sq}^{-1}$, supported by optically transparent PMMA boards with thicknesses of $h_B = 12\,\text{mm}$, $h_{C1} = 6\,\text{mm}$, and $h_{C2} = 5.4\,\text{mm}$, as shown in Figures S2–S3. The continuously grown MWCNTF was etched onto the optically transparent PMMA board using laser etching technology, with an aluminum board of the same size on the bottom. Far-field measurements were conducted in a standard microwave anechoic chamber, with the positions of the transmitting antenna, receiving antenna, and sampling shown in Figure 5(d). The operating frequency band of the antenna is 8–12 GHz. Initially, the transmitting antenna was fixed at a 15° position on the left side of the bow-shaped support, while the receiving antenna moved along the scanning trajectory on the right side of the bow-shaped support in 5° increments, especially at the angle of the desired direction. The signal reflected from the metasurface was mea-

TABLE 2. Comparison of ASIMMS with prior metasurface designs.

Reference	Absorption/Reflection Efficiency	Incidence/Reflection Angle Range	Mechanism
[7]	absorption $> 90\%$	limited by normal incidence	absorption
[23]	reflection $> 76\%$	$\theta = 88°$	reflection
[35]	reflection $= 94\%$	$\theta = 70°$	reflection
[36]	absorption $= 99.95\%$	the incidence angles were $45°$ and $0°$	no simultaneous control of absorption and scattering
[42]	reflection $= 91.2\%$	$\theta = 70°$	reflection
This work	97.9% (11.1% of anomalous reflection)	$\theta = 77.5°$ (under $15°$ oblique incidence)	Integrates absorption and scattering

sured by the receiving antenna at different angles. However, due to the antennas not being able to move to the same side of the bow-shaped support, the reflection signal at the negative reflection angle of 15° incidence could not be measured, but according to the simulation, these signals should be at a very low level. As shown in Figures 5(e) and (f), the main reflection peaks of the three metasurfaces both occur at 15° and 62.5°, which are the expected results of the theory and simulation.

To estimate the amplitude efficiency of the metasurfaces $n = 0$ and $n = 1$ order channels, we replaced the metasurface with an aluminum plate of the same size and measured the received signals of the specular reflection with incident angles of $\theta_i = 15°$ and 39° (θ/2). To find the reflection efficiency of the metasurface under different channels, we normalized its signal amplitude $|S^0_{21,m}|$ for $\theta/2 = 15°$ and $|S^1_{21,m}|$ for $\theta/2 = 39°$. Since the angle between the transmitting and receiving antennas is the same as the reflection angle of the metasurface, the reflection signal amplitude of the reference uniform metal mirror under different incident angles θ/2 was used for normalization. Additionally, we divided the obtained amplitudes by the estimated correction factor [35] $\xi_0 = \sqrt{\cos(\theta)}/Mcos(\theta/2)$. The correction factor ξ_0 is less than 1, because, in this case, due to the different relative directions with respect to the antenna, the radiation effective area of an ideal wire plate is greater than that of an ideal reflecting metasurface. As shown in Figures 5(g)–(i), at the designed frequency of 10 GHz, the correction factor is $\xi_0 = 0.9$, and the reflection efficiencies of the metasurfaces designed by the three schemes at 15° and 62.5° ($n = 0$, $n = 1$) are $\xi_{a,0} = 77.4\%$ and $\xi_{a,1} = 0.7\%$, $\xi_{b,0} = 27.8\%$ and $\xi_{b,1} = 1.8\%$, $\xi_{c,0} = 1.5\%$ and $\xi_{c,1} = 10.2\%$, respectively. The consistency between experimental results and simulation data validates the rationality and effectiveness of the high-efficiency ASIMMS design.

During the fabrication process, errors in processing may result in deviations between the true surface morphology of the diffractive optical element's microstructure and the specified design parameters. Moreover, the edge period width of the microstructure surface is small, which introduces shading errors when being obliquely incident, leading to deviations between the measured diffraction efficiency and theoretical values. In Scheme 3, the tested reflection efficiencies for $n = 0$ and $n = 1$ orders are almost equal to the simulated results, validating the capability of the ASIMMS. This result further confirms that under oblique incidence, the metasurface perfectly absorbs the energy of parasitic reflections and reflects all the remaining power at the desired angle of 62.5°. As shown in Figure 5(i), when the frequency is below 9 GHz, the MWCNT bars on the substrate are weakly excited. Even at frequencies below 8.4 GHz, the metasurface behaves as a conventional mirror, following simple reflection laws. This is because the abnormal reflection angle in the $n = 0$ mode at oblique incidence depends on Eq. (3), being 62.5° at 10 GHz and varying from 90° to 51.2° as the frequency changes from 8 GHz to 12 GHz. Therefore, in order to evaluate the reflection efficiency in the anomalous direction across various frequencies, we employed received signals at different angles (Section S4). Despite minor fluctuations on the curve due to discrete angle scanning steps during measurement, the observed efficiency is consistent with the results of numerical simulations.

Table 2 compares our results with those of previous studies. The most prominent advantage of the proposed ASIMMS lies in its ability to reduce parasitic reflections under oblique incidence and achieve highly efficient integration of absorption and scattering. Moreover, the scattering angle is larger than that in previous works, and the absorption-scattering efficiency reaches 97.9%, which is superior to other studies. Thus, the outstanding performance of the proposed ASIMMS has been verified.

5. CONCLUSION

In this study, we successfully designed and experimentally verified a novel multifunctional ASIMMS, which can effectively control the propagation and absorption of electromagnetic waves by precise impedance modulation. MWCNTF is used in metasurface design, using its high electrical conductivity to enhance the localization of electromagnetic fields within the metasurface, thereby increasing absorption efficiency. The experimental results demonstrate the effectiveness of the designed ASIMMS and the application of the semi-analytical method in engineering multifunctional absorption and reflection integrated metasurface. The method effectively utilizes the evanescent wave mechanism to precisely control the direction and amplitude of scattering, paving the way for innovative applications of beam manipulation and control.

6. SUPPORTING INFORMATION

Supporting Information is available from the authors.

7. EXPERIMENTAL SECTION

Finite Element Simulation of Electromagnetic Properties: electromagnetic simulations of MWCNTF were conducted using COMSOL Multiphysics 6.1 software. Transition boundary conditions were employed to simulate the electromagnetic behavior of the metal/MWCNT layer, utilizing complex wave numbers and complex impedance to describe the local electric field intensity distribution of MWCNTs, with material conductivity set to 7×10^4 S/m, wall thickness of $s = 0.34$ nm, and MWCNT diameter of $d = 40$ nm.

Microscopic Characterization: the microstructure of MWCNTF was characterized using scanning electron microscopy (SEM) to obtain images of the MWCNTF and measure the diameter of individual MWCNTF. Optical images were captured using an industrial microscope. SEM images were acquired using a ZEISS GeminiSEM 360 device. Raman spectra were obtained using a RENISHAW INVIA0117-13 instrument with 532 nm laser excitation and a $50x$ objective.

Electrical and Electromagnetic Measurements: the resistivity of the MWCNT film was measured using a four-point probe resistivity measurement system (RTS-8). In the frequency range of 8.2–12.4 GHz, the electromagnetic parameters of MWCNTF, including dielectric constant, electromagnetic reflectance, absorption, and transmittance, were evaluated using a vector network analyzer (Ceyear 3672C-S) and waveguide method.

Metasurface Design and Modeling: a metasurface prototype designed to operate at a specific frequency of 10 GHz was created. The impedance sheet of the metasurface was discretized into multiple sub-cells, with each further divided into smaller sub-sub-cells. The effective grid impedance of each sub-sub-cell was retrieved from the simulated reflection coefficient (S_{11}) using the locally periodic approximation and transmission-line method approach. Numerical simulations were carried out using a frequency-domain solver in CST Microwave Studio 2020, with excitations propagating along the z-direction from port one, with the electric field along the y-direction and the magnetic field along the x-direction to obtain the S_{11} parameter. All elements in the unit cells were designed and optimized one by one to fit the theoretically required surface impedance. Once the dimensions of all elements in the unit cells were determined, numerical simulations for 15° incidence were performed. The complete unit cell simulation domain and boundary conditions, along with Floquet ports, were set. The scattered fields for 15° oblique incidence were calculated by subtracting the incident waves from the total fields.

Fabrication and Measurement: the periodic array pattern of the metasurface was fabricated on copper foil/FR4 and MWCNTF using printed circuit board technology and laser etching technology, respectively. The sample consists of multiple unit cells with dimensions of $12.8\lambda \times 7.3\lambda = 348$ mm $\times 220$ mm, adhered to a SiO_2 substrate with a dielectric constant of $\epsilon = 3.94(1 + j0.0002)$ and a PMMA substrate with a dielectric constant of $\epsilon = 2.65(1 + j0.0057)$, backed by an aluminum plate.

The designed metasurface was tested using a bow-shaped support and a vector network analyzer. In the experiment, two high-gain double-ridge horn antennas connected to a vector network analyzer served as the transmitter and receiver. The metasurface was positioned at a specific distance from both the transmitting and receiving antennas, where the radiation from the antennas can be approximated as a plane wave. The antennas were moved along a scanning trajectory to measure reflections at different angles. Time gating was employed to filter out all the multiple scattering noise signals received by the antenna.

ACKNOWLEDGEMENT

This work was supported by the National Natural Science Foundation of China (Grant No. 52071294 and 52471212), Natural Science Foundation of Zhejiang Province (Grant LY20E020015), and the National Key Research and Development Program (Grant No. 2022YFE0109800).

REFERENCES

[1] Marin, P., D. Cortina, and A. Hernando, "Electromagnetic wave absorbing material based on magnetic microwires," *IEEE Transactions on Magnetics*, Vol. 44, No. 11, 3934–3937, 2008.

[2] Dai, J. Y., J. Zhao, Q. Cheng, and T. J. Cui, "Independent control of harmonic amplitudes and phases via a time-domain digital coding metasurface," *Light: Science & Applications*, Vol. 7, No. 1, 90, 2018.

[3] Grant, J., Y. Ma, S. Saha, L. B. Lok, A. Khalid, and D. R. S. Cumming, "Polarization insensitive terahertz metamaterial absorber," *Optics Letters*, Vol. 36, No. 8, 1524–1526, 2011.

[4] Zhu, X., J. Xu, F. Qin, Z. Yan, A. Guo, and C. Kan, "Highly efficient and stable transparent electromagnetic interference shielding films based on silver nanowires," *Nanoscale*, Vol. 12, No. 27, 14 589–14 597, 2020.

[5] Asadchy, V. S., A. Díaz-Rubio, S. N. Tcvetkova, D.-H. Kwon, A. Elsakka, M. Albooyeh, and S. A. Tretyakov, "Flat engineered multichannel reflectors," *Physical Review X*, Vol. 7, No. 3, 031046, 2017.

[6] Hu, F. and A. Epstein, "Large-aperture cavity-excited metagrating antennas for dynamic beam switching," in *2023 International Workshop on Antenna Technology (iWAT)*, 1–4, Aalborg, Denmark, May 2023.

[7] Tan, Z., J. Yi, Q. Cheng, and S. N. Burokur, "Design of perfect absorber based on metagratings: Theory and experiment," *IEEE Transactions on Antennas and Propagation*, Vol. 71, No. 2, 1832–1842, 2023.

[8] He, T., T. Liu, S. Xiao, Z. Wei, Z. Wang, L. Zhou, and X. Cheng, "Perfect anomalous reflectors at optical frequencies," *Science Advances*, Vol. 8, No. 9, eabk3381, 2022.

[9] Kwon, D.-H., "Lossless scalar metasurfaces for anomalous reflection based on efficient surface field optimization," *IEEE Antennas and Wireless Propagation Letters*, Vol. 17, No. 7, 1149–1152, 2018.

[10] Rabinovich, O., Y. Komarovsky, D. Dikarov, and A. Epstein, "Printed circuit board (PCB) metagratings for perfect anomalous refraction: Theory and experiment," in *2019 International Conference on Electromagnetics in Advanced Applications (ICEAA)*, 1070–1070, Granada, Spain, 2019.

[11] Shklarsh, Y. and A. Epstein, "Semianalytically designed dual-polarized printed-circuit-board (PCB)-compatible metagratings," *IEEE Transactions on Antennas and Propagation*, Vol. 72, No. 2, 1397–1406, 2024.

[12] Haddad, H., R. Loison, R. Gillard, A. Harmouch, and A. Jrad, "Mitigation of parasitic reflections over periodic surface impedance modulated panels," in *2019 13th European Conference on Antennas and Propagation (EuCAP)*, 1–4, Krakow, Poland, Mar.–Apr. 2019.

[13] Yashno, Y. and A. Epstein, "Large-period multichannel metagratings for broad-angle absorption," in *2022 Sixteenth International Congress on Artificial Materials for Novel Wave Phenomena (Metamaterials)*, X–134, Siena, Italy, Sep. 2022.

[14] Movahediqomi, M., G. Ptitcyn, and S. Tretyakov, "Comparison between different designs and realizations of anomalous reflectors for extreme deflections," *IEEE Transactions on Antennas and Propagation*, Vol. 71, No. 10, 8007–8017, 2023.

[15] Pan, W., Z. Wang, Y. Chen, X. Zheng, S. Li, X. Tian, Q. He, L. Zhou, and S. Sun, "Efficiently controlling near-field wavefronts via designer metasurfaces," *ACS Photonics*, Vol. 10, No. 7, 2423–2431, 2023.

[16] Fang, Z., H. Li, Y. Chen, S. Sun, S. Xiao, Q. He, and L. Zhou, "Deterministic approach to design passive anomalous-diffraction metasurfaces with nearly 100% efficiency," *Nanophotonics*, Vol. 12, No. 13, 2383–2396, 2023.

[17] Wang, X., G. Ptitcyn, V. S. Asadchy, A. Díaz-Rubio, M. S. Mirmoosa, S. Fan, and S. A. Tretyakov, "Nonreciprocity in bianisotropic systems with uniform time modulation," *Physical Review Letters*, Vol. 125, No. 26, 266102, 2020.

[18] Hoffmann, A. and D. Manteuffel, "Investigation of modeling of anomalous reflecting metasurfaces using characteristic modes," in *2022 International Workshop on Antenna Technology (iWAT)*, 125–127, Dublin, Ireland, May 2022.

[19] Zang, Y., R. Chai, W. Liu, Z. Li, H. Cheng, J. Tian, and S. Chen, "Enhanced wide-angle third-harmonic generation in flat-band-engineered quasi-BIC metagratings," *Science China Physics, Mechanics & Astronomy*, Vol. 67, No. 4, 244212, 2024.

[20] Kim, M., A. M. H. Wong, and G. V. Eleftheriades, "Optical Huygens' metasurfaces with independent control of the magnitude and phase of the local reflection coefficients," *Physical Review X*, Vol. 4, No. 4, 041042, 2014.

[21] Zheng, G., H. Muhlenbernd, M. Kenney, G. Li, T. Zentgraf, and S. Zhang, "Metasurface holograms reaching 80% efficiency," *Nature Nanotechnology*, Vol. 10, No. 4, 308–312, 2015.

[22] Yang, W., J. Qin, J. Long, W. Yan, Y. Yang, C. Li, E. Li, J. Hu, L. Deng, Q. Du, and L. Bi, "A self-biased non-reciprocal magnetic metasurface for bidirectional phase modulation," *Nature Electronics*, Vol. 6, No. 3, 225–234, 2023.

[23] Estakhri, N. M. and A. Alù, "Wave-front transformation with gradient metasurfaces," *Physical Review X*, Vol. 6, No. 4, 041008, 2016.

[24] Sun, S., K.-Y. Yang, C.-M. Wang, T.-K. Juan, W. T. Chen, C. Y. Liao, Q. He, S. Xiao, W.-T. Kung, G.-Y. Guo, L. Zhou, and D. P. Tsai, "High-efficiency broadband anomalous reflection by gradient meta-surfaces," *Nano Letters*, Vol. 12, No. 12, 6223–6229, 2012.

[25] Xu, H.-X., G. Hu, X. Kong, Y. Shao, P. Genevet, and C.-W. Qiu, "Super-reflector enabled by non-interleaved spin-momentum-multiplexed metasurface," *Light: Science & Applications*, Vol. 12, No. 1, 78, 2023.

[26] Marcus, S. W. and A. Epstein, "Omega bianisotropic metasurfaces as Huygens' metasurfaces with anti-reflective coatings," in *2020 Fourteenth International Congress on Artificial Materials for Novel Wave Phenomena (Metamaterials)*, 361–363, New York, NY, USA, Sep. 2020.

[27] Xiong, L., P. Chai, A. Fu, Y. Fu, R. Tan, and P. Chen, "Design of a multifunctional metasurface with frequency-selective absorbing properties," in *2023 IEEE International Workshop on Electromagnetics: Applications and Student Innovation Competition (iWEM)*, 130–132, Harbin, China, Jul. 2023.

[28] Jain, P., A. K. Singh, J. K. Pandey, S. Garg, S. Bansal, M. Agarwal, S. Kumar, N. Sardana, N. Gupta, and A. K. Singh, "Ultrathin metamaterial perfect absorbers for single-/dual-/multi-band microwave applications," *IET Microwaves, Antennas & Propagation*, Vol. 14, No. 5, 390–396, 2020.

[29] Marcus, S. W., V. K. Killamsetty, Y. Yashno, and A. Epstein, "Multimodal antireflective coatings for perfecting anomalous reflection from arbitrary periodic structures," *Physical Review B*, Vol. 106, No. 20, 205132, 2022.

[30] Marcus, S. W. and A. Epstein, "Coated phase-gradient metasurfaces for perfect anomalous reflection," in *2021 Fifteenth International Congress on Artificial Materials for Novel Wave Phenomena (Metamaterials)*, 242–244, New York, NY, USA, Sep. 2021.

[31] Rahmanzadeh, M. and A. Khavasi, "Perfect anomalous reflection using a compound metallic metagrating," *Optics Express*, Vol. 28, No. 11, 16 439–16 452, 2020.

[32] Epstein, A. and O. Rabinovich, "Unveiling the properties of metagratings via a detailed analytical model for synthesis and analysis," *Physical Review Applied*, Vol. 8, No. 5, 054037, 2017.

[33] Rabinovich, O. and A. Epstein, "Analytical design of printed circuit board (PCB) metagratings for perfect anomalous reflection," *IEEE Transactions on Antennas and Propagation*, Vol. 66, No. 8, 4086–4095, 2018.

[34] Epstein, A. and G. V. Eleftheriades, "Synthesis of passive lossless metasurfaces using auxiliary fields for reflectionless beam splitting and perfect reflection," *Physical Review Letters*, Vol. 117, No. 25, 256103, 2016.

[35] Díaz-Rubio, A., V. S. Asadchy, A. Elsakka, and S. A. Tretyakov, "From the generalized reflection law to the realization of perfect anomalous reflectors," *Science Advances*, Vol. 3, No. 8, e1602714, 2017.

[36] Zhong, S., X. Wang, and S. A. Tretyakov, "Coherent control of wave beams via unidirectional evanescent modes excitation," *Advanced Functional Materials*, Vol. 33, No. 48, 2304300, 2023.

[37] Ando, T., "The electronic properties of graphene and carbon nanotubes," *NPG Asia Materials*, Vol. 1, No. 1, 17–21, 2009.

[38] Li, B., Y. Yang, N. Wu, S. Zhao, H. Jin, G. Wang, X. Li, W. Liu, J. Liu, and Z. Zeng, "Bicontinuous, high-strength, and multifunctional chemical-cross-linked MXene/superaligned carbon nanotube film," *ACS Nano*, Vol. 16, No. 11, 19 293–19 304, 2022.

[39] Wu, Y., S. Tan, G. Fang, Y. Zhang, and G. Ji, "Manipulating CNT films with atomic precision for absorption effectiveness–enhanced electromagnetic interference shielding and adaptive infrared camouflage," *Advanced Functional Materials*, 2402193, 2024.

[40] Wang, Y., G. Duan, L. Zhang, L. Ma, X. Zhao, and X. Zhang, "Terahertz dispersion characteristics of super-aligned multi-walled carbon nanotubes and enhanced transmission through subwavelength apertures," *Scientific Reports*, Vol. 8, No. 1, 2087, 2018.

[41] Huang, K., F. Liang, J. Sun, Q. Zhang, Z. Li, S. Cheng, W. Li, H. Yuan, R. Liu, Y. Ge, *et al.*, "Overcoming the incompatibility between electrical conductivity and electromagnetic transmissivity: A graphene glass fiber fabric design strategy," *Advanced Materials*, Vol. 36, No. 24, 2313752, 2024.

[42] Jing, H. B., Q. Ma, G. D. Bai, and T. J. Cui, "Anomalously perfect reflections based on 3-bit coding metasurfaces," *Advanced Optical Materials*, Vol. 7, No. 9, 1801742, 2019.

[43] Asadchy, V. S., M. Albooyeh, S. N. Tcvetkova, A. Díaz-Rubio, Y. Ra'di, and S. A. Tretyakov, "Perfect control of reflection and refraction using spatially dispersive metasurfaces," *Physical Review B*, Vol. 94, No. 7, 075142, 2016.

[44] Wang, X., A. Díaz-Rubio, and S. A. Tretyakov, "Independent control of multiple channels in metasurface devices," *Physical Review Applied*, Vol. 14, No. 2, 024089, 2020.

[45] Liu, L., X. Zhang, M. Kenney, X. Su, N. Xu, C. Ouyang, Y. Shi, J. Han, W. Zhang, and S. Zhang, "Broadband metasurfaces with simultaneous control of phase and amplitude," *Advanced Materials*, Vol. 26, No. 29, 5031–5036, 2014.

[46] Qi, C. and A. M. H. Wong, "Broadband efficient anomalous reflection using an aggressively discretized metasurface," *Optics Express*, Vol. 30, No. 9, 15 735–15 746, 2022.